

1     **Constraining spectral models of a terrestrial gamma-ray**  
2     **flash from a terrestrial electron beam observation by the**  
3     **Atmosphere-Space Interactions Monitor**

4     **D. Sarria<sup>1</sup>, N. Østgaard<sup>1</sup>, P. Kochkin<sup>1</sup>, N. Lehtinen<sup>1</sup>, A. Mezentsev<sup>1</sup>, M.**  
5     **Marisaldi<sup>1</sup>, A. Lindanger<sup>1</sup>, C. Maiorana<sup>1</sup>, B. E. Carlson<sup>1,2</sup>, T. Neubert<sup>3</sup>, V.**  
6     **Reglero<sup>4</sup>, K. Ullaland<sup>1</sup>, S. Yang<sup>1</sup>, G. Genov<sup>1</sup>, B. H. Qureshi<sup>1</sup>, C.**  
7     **Budtz-Jørgensen<sup>3</sup>, I. Kuvvetli<sup>3</sup>, F. Christiansen<sup>3</sup>, O. Chanrion<sup>3</sup>, J.**  
8     **Navarro-González<sup>4</sup>, P. Connel<sup>4</sup>, C. Eyles<sup>4</sup>**

9             <sup>1</sup>Birkeland Centre for Space Science, University of Bergen, Bergen, Norway

10            <sup>2</sup>Carthage College, Kenosha, Wisconsin, United States

11            <sup>3</sup>National Space Institute, Technical University of Denmark, Lyngby, Denmark

12            <sup>4</sup>University of Valencia, Valencia, Spain

13     **Key Points:**

- 14     • Observation of a Terrestrial Electron Beam with a spectrum resolved down to 50  
15     keV
- 16     • A method to constrain the energy spectrum of the source Terrestrial Gamma-ray  
17     Flash based on the detection of the associated TEB is presented
- 18     • Only TGFs originating from fully-developed RREA models can explain the ob-  
19     servation

**Abstract**

Terrestrial Gamma-ray Flashes (TGFs) are short flashes of high energy photons, produced by thunderstorms. When interacting with the atmosphere, they produce relativistic electrons and positrons, and a part gets bounded to geomagnetic field lines and travels large distances in space. This phenomenon is called a Terrestrial Electron Beam (TEB). The Atmosphere-Space Interactions Monitor (ASIM) mounted on-board the International Space Station detected a new TEB event on March 24, 2019, originating from the tropical cyclone Johanina. Using ASIM's low energy detector, the TEB energy spectrum is resolved down to 50 keV. We provide a method to constrain the TGF source spectrum based on the detected TEB spectrum. Applied to this event, it shows that only fully developed RREA spectra are compatible with the observation. More specifically, assuming a TGF spectrum  $\propto E^{-1} \exp(-E/\epsilon)$ , the compatible models have  $\epsilon \geq 6.5$  MeV ( $E$  is the photon energy and  $\epsilon$  is the cut-off energy). We could not exclude models with  $\epsilon$  of 8 and 10 MeV.

**Plain Language Summary**

Terrestrial Gamma-ray Flashes (TGF), originating from thunderstorms, are the highest energy natural particle acceleration phenomena occurring on Earth. The production mechanism of TGFs is not very well understood. When interacting with the atmosphere, TGFs produce secondary electrons and positrons, and a part gets bounded to Earth's magnetic field lines, and travels large distances in space. They can be detected by instruments on-board satellites located at the right place (in a window of about 40 km) at the right time (in a window of a few milliseconds). This phenomenon is called a Terrestrial Electron Beam (TEB). By detecting the TEB, we can retrieve information about the TGF that produced it. In this article we present the first TEB originating from a tropical cyclone, and with the lowest energies ever recorded (down to 50 keV). We also provide a method to infer properties of the energy distribution of the TGF (producing the TEB) based on the energy spectrum of the TEB. Applied to this event, it shows that only TGF energy spectra among the most energetic that were proposed are compatible, and we cannot exclude even more energetic events.

## 1 Introduction

Terrestrial Gamma-ray Flashes (TGFs) are short bursts of high energy ( $< 40$  MeV) photons, produced during thunderstorms. A review of TGFs theory and observations is presented by Dwyer et al. (2012). TGFs were first detected using the BATSE experiment on-board the CGRO spacecraft (Fishman et al., 1994). Later, TGFs were recorded by the satellites RHESSI (Smith et al., 2005), AGILE (Marisaldi et al., 2014), Fermi (Briggs et al., 2010; Roberts et al., 2018), BeppoSAX (Ursi et al., 2017) and the Atmosphere-Space Interactions Monitor (ASIM) (Neubert, Østgaard, Reglero, Blanc, et al., 2019). ASIM was successfully launched and docked to the International Space Station in April 2018, and started science operations since June 2018. The first results from ASIM were presented by Østgaard, Neubert, et al. (2019); Sarria et al. (2019); Neubert, Østgaard, Reglero, Chanrion, et al. (2019).

When referring to "electrons beams" in the context of TGFs, one can think of two different objects. The first is associated with the production process of the TGF. This production process takes place, at least for TGF detectable from space, between  $\approx 10$  and  $\approx 15$  km altitude. This first type of "electron beam" consists of the Relativistic Runaway Electron Avalanche (RREA) producing the TGF's high energy photons. This RREA is not detectable from space since it is impossible for it to go through the atmosphere layer. The second type of "electron beam" is called "terrestrial electron beam" (TEB) and is produced higher in the atmosphere by the TGF's photons, though the processes of Compton scattering and electron-positron pair production. Since electron-positron pair production is involved, TEBs are composed of a fraction of positrons, typically 10 % to 30 % (see Briggs et al. (2011), table 1). A TEB is bound ("beamed") around the magnetic field line intercepting the source TGF's geographical location (Dwyer et al., 2008; Cohen et al., 2010; Sarria et al., 2015). Most electrons and positrons forming TEBs are produced above 40 km altitude, where the air collision frequency of the electrons (and positrons) is comparable to their gyration frequency around geomagnetic field lines. TEBs propagate in space and travel large distances in the magnetosphere. TEBs were first reported from measurements of the CGRO spacecraft (Dwyer et al., 2008). Later, they were detected by Fermi (Briggs et al., 2011; Stanbro et al., 2019), BeppoSAX (Ursi et al., 2017), AGILE (Lindanger et al., 2020) and ASIM (Sarria et al., 2019). RHESSI probably detected one or two TEB event(s), but it has not been 100% confirmed yet (Smith et al., 2006; Gjesteland, 2012). In general, TEBs are detected much less often than TGFs (e.g.

82 Fermi has a few thousand TGFs and about 30 TEBs) because the detector must be lo-  
83 cated inside a narrow window of less than a few tens of kilometers along the right ge-  
84 omagnetic field line (intercepting the TGF source position), and they last for only a few  
85 milliseconds.

86 One of the reasons of studying TEBs is to retrieve information about the TGFs that  
87 produced them. Briggs et al. (2011) constrained the positron fraction to be between 10  
88 and 34%, based on 3 events. Positrons fractions are linked to the spectral shape of the  
89 source TGF, as photons with harder spectrums will do more pair production. In Sarria  
90 et al. (2019), the beaming of the source TGF could be constrained between about  $30^\circ$   
91 and  $42^\circ$  (half angle, isotropic within a cone). Another reason to study TEBs is that they  
92 may have an impact on the inner Van Allen radiation belt, that has not been quantified  
93 yet (to our knowledge). Even if it is an important question, it is not the subject of the  
94 present paper.

95 One of the most important question regarding TGFs is their production mechanism.  
96 Two main models are proposed to explain the production of TGFs, and in both, the TGF's  
97 photons are produced by high energy electrons through the bremsstrahlung process. These  
98 high energy electrons form a Relativistic Runaway Electron Avalanche (RREA) (Wilson,  
99 1924; Gurevich et al., 1992). In the first model, a large scale electric field within thun-  
100 derclouds is considered. This requires the presence of initial high energy seed electrons,  
101 that may be provided by cosmic-ray secondaries or background radiation. The background  
102 electric field is strong enough to produce RREA avalanches, but the RREA mechanism  
103 alone is not enough to produce bright enough TGFs (i.e. detectable from space, there-  
104 fore with more than  $10^{16}$  photons between 50 keV and 40 MeV at source), and a x-ray  
105 and positron feedback mechanism is required (the "relativistic feedback"); only possi-  
106 ble if large potentials are available (Dwyer et al., 2003; Babich et al., 2005; Dwyer, 2012;  
107 Skeltved et al., 2014). This mechanism will produce a discharge of the thundercloud, that  
108 is of different nature than usual lightning discharges. The resulting high-energy photon  
109 spectrum given by this model is a so-called "fully-developed" RREA. The development  
110 of a RREA process can be characterized by the number of avalanche lengths that were  
111 achieved (that depends on the extend and magnitude of the available electric potential).  
112 The energy spectrum of the electrons converges to a standard shape ( $\approx \exp(-E/7.3\text{MeV})$ ),  
113 which is fully obtained with six or more avalanche lengths, even if the total number of  
114 electrons keeps exponentially increasing with the number of avalanche lengths. Another

115 variant of this model uses a lightning leader to push the background (large scale) field  
116 above the threshold to trigger the relativistic feedback mechanism (Skeltved et al., 2017).

117 The second model of TGF production requires a propagating lightning leader. It  
118 is sometimes referred as the "leader-streamer" model. It considers that initial seed elec-  
119 trons are produced by the cold runaway mechanism (Gurevich, 1961), happening in the  
120 streamer phase or in the leader phase (Moss et al., 2006; Dwyer, 2008; Celestin & Pasko,  
121 2011; Chanrion et al., 2014; Kohn & Ebert, 2015). These energetic seed electrons follow  
122 a specific distribution and a fraction of them are then accelerated and multiplied by a  
123 larger scale electric field, producing a RREA. The larger scale electric field can be the  
124 field induced by the leader and/or a large scale (background) field in the thunderstorm.  
125 In principle, leader-based TGF production models do not exclude the possibility of rel-  
126 ativistic feedback, that could be more or less important (Skeltved et al., 2017). A pa-  
127 rameter that impacts the energy spectrum of emitted photons the most is the potential  
128 drop in the leader tip region that is available for the acceleration of energetic electrons.  
129 Resulting TGF energy spectra for several leader potential drops are presented in Celestin  
130 et al. (2015), figure 3. They actually correspond to a more or less developed RREA pro-  
131 cess. Celestin et al. (2012) also showed that energy spectra harder than this character-  
132 istic fully-developed RREA spectrum could be achieved by involving non-equilibrium ac-  
133 celeration of electrons. One significant advantage of leader-based TGF models is that  
134 they propose an unified approach to explain TGF's X/gamma-ray production, as well  
135 as x-ray (i.e. softer) emissions from lightning propagating leaders, that were observed  
136 from ground, balloons and aircraft (Dwyer et al., 2003, 2004, 2005, 2011). Mailyan et  
137 al. (2019) presented the first study that confronted leader models to TGFs recorded by  
138 the Fermi space telescope, with tested potential drops  $\leq 200$  MV. They found that light-  
139 ning leader models with potentials of 200 MV and tilted beams gave the best fit to the  
140 data in most of the analyzed TGF events. However, the range of compatible models is  
141 found to be quite wide.

142 In this article, we report the second TEB event detected by ASIM on 24 March 2019.  
143 Compared to the previous event (presented in Sarria et al. (2019)), data from the two  
144 detectors are available: the pixelated Low-Energy detector (50-400 keV) and the High  
145 Energy Detector (300 keV-30 MeV), that permits an unprecedented spectral analysis of  
146 a TEB event. In section 2, we present the instruments that were used. In section 3 we

147 present the event. In section 4 we present the methods and models we use for the spec-  
148 tral analysis. In section 5 we show the results of the analysis. We conclude in section 6.

## 149 2 Instruments

150 The ASIM payload (Neubert, Østgaard, Reglero, Blanc, et al., 2019) consists of two  
151 main instruments, the Modular X- and Gamma-ray Sensor (MXGS) (Østgaard, Balling,  
152 et al., 2019) and the Modular Multi-spectral Imaging Array (MMIA) (Chanrion et al.,  
153 2019). ASIM is mounted on the International Space Station (ISS) orbiting the Earth at  
154 about 400 kilometers altitude with an inclination of  $51.6^\circ$ . MXGS consists of two detec-  
155 tors for detecting X- and gamma-rays. The MXGS Low-Energy Detector (LED) is layer  
156 of 16384 pixels of Cadmium-Zink-Telluride (CZT) detector crystals, sensitive to photons  
157 with energies from 50 keV to about 400 keV. The MXGS High Energy Detector (HED)  
158 comprises 12 Bismuth-Germanium-Oxide (BGO) detector modules coupled to photomul-  
159 tiplier tubes (PMT), sensitive in the energy range of 300 keV to about 40 MeV.

160 GLD360 (VAISALA) is a network of ground-based lightning sensors (1 kHz-350 kHz)  
161 detecting both Cloud-to-Ground and Intra-Cloud lightning. The GLD360 sensors use a  
162 combination of magnetic direction finding and time-of-arrival calculations (from 4 sta-  
163 tions or more) to geolocate the lightning source (see acknowledgments for more details).  
164 The typical uncertainty on location is about 2.5 km and it can vary a lot with geograph-  
165 ical location (Rudlosky et al., 2017).

166 We also present data provided by the Meteosat-11 geostationary satellite, that pro-  
167 vides regular scans of cloud coverage at several wavelengths (used data comes from band  
168 4, at  $3.9 \mu\text{m}$ , with a 3 km spatial resolution). See acknowledgments for more informa-  
169 tion.

## 170 3 Observation

171 Figure 1 shows a map of the event together with Satellite imagery that was pro-  
172 vided by the geostationary satellite Meteosat-11. The ASIM trigger UTC time is 2019-  
173 Mar-24 00:31:53.135444 and the ISS was located at latitude of  $\phi = 0.157^\circ$ , longitude  
174 of  $\lambda = 55.301^\circ$  and altitude of  $h = 408.6$  km, that is above the Indian ocean, close to  
175 Madagascar. The ASIM clock has a -20 to 30 ms absolute timing uncertainty with re-  
176 spect to GPS UTC time. A VAISALA (GLD360) discharge event with a UTC time of

177 2019-03-24 00:31:53.134000 ( $\Delta t = 1.44$  ms) was found very close to the southern mag-  
 178 netic line footpoint (at 45 km altitude) intercepting the ISS position : [ $\phi_{GLD360} = -7.049^\circ$ ,  
 179  $\lambda_{GLD360} = 55.912^\circ$ ] and [ $\phi_{mag,s} = -7.007^\circ$ ,  $\lambda_{mag,s} = 55.923^\circ$ ] that gives  $\Delta r = 4.82$  km.  
 180 Note that the GLD360 location uncertainty can be up to 20 km for this event, and the  
 181 uncertainty in the ISS position is of the same order. The northern magnetic field line  
 182 footpoint is located at [ $\phi_{mag,n} = 20.524^\circ$ ,  $\lambda_{mag,n} = 55.099^\circ$ ], but no lightning activ-  
 183 ity was observed close to it. No lightning activity was detected by GLD360 below the  
 184 ISS, within 540 km and  $\pm 1$  second around the trigger time. The MMIA photometers did  
 185 not detect any lightning activity below the ISS as well.

186 From satellite imagery (figure 1), it appears that the southern magnetic field line  
 187 footpoint is located in the rainbands of a tropical cyclone, named "Joaninha". It is the  
 188 first time that the detection of a TEB associated to a TGF produced in a cyclone is re-  
 189 ported.

190 Figure 2.a shows the recorded lightcurves for LED and HED, as well as a model-  
 191 ing result. The latter is obtained using what will be referred as the "consensus model",  
 192 that assumes a source TGF located at the southern magnetic footpoint, at 12 km alti-  
 193 tude, with an angular distribution following a Gaussian distribution with  $\sigma_\theta = 20^\circ$  (cen-  
 194 tered on zenith), and with an energy spectrum  $\propto E^{-1} \exp(-E/7.3 \text{ MeV})$  (maximum  
 195 energy set to 40 MeV). More information about the modeling is presented in the next  
 196 section. The consensus model gives a very good fit to the data (see figure label). Fig-  
 197 ure 2.b shows the spectra recorded by the MXGS instrument for LED and HED. There  
 198 is a total of 168 counts in HED and 307 counts in LED. The error bars are  $1-\sigma$  ( $\approx 68$  %  
 199 interval) assuming Poisson statistics on the count values given by the model. The spec-  
 200 trum shows a strong line at 511 keV, that is expected because the electron beams con-  
 201 tains a significant fraction of positrons. The consensus model gives a very good fit to the  
 202 spectral data as well (see figure label), and a positron to electron ratio of 16.1 %. This  
 203 value is comparable to previous results (Briggs et al., 2011).

#### 204 **4 Method to constrain the source TGF spectrum**

205 As presented in the introduction, for any considered TGF production scenario, the  
 206 spectral shape for the TGF is governed by the RREA process that produces high-energy  
 207 photons through the bremsstrahlung process. A RREA can be more or less developed

208 depending on how many avalanches lengths have been achieved, that depends on the avail-  
 209 able potential (in the leader and/or background electric field) and the extend of the elec-  
 210 tric field(s). When the RREA process is close to being fully developed, the resulting TGF  
 211 photon energy spectrum can be well approximated with equation 1:

$$f(E) \propto E^{-1} \exp(-E/\epsilon), \text{ with } E < E_m \quad (1)$$

212 Where  $E$  is the energy,  $\epsilon$  is a cut-off energy and  $E_m$  is the maximum allowed en-  
 213 ergy. TGF energy spectra from fully-developed RREA are expected to have  $\epsilon \geq 5$  MeV  
 214 (Dwyer, 2012; Skeltved et al., 2014; Sarria et al., 2018). Typical TGFs spectra used in  
 215 the literature have  $\epsilon = 6.5$  to  $7.3$  MeV, with  $E_m$  of  $30$  to  $40$  MeV. TGF production mod-  
 216 els based on a propagating lightning leader can, in theory, produce bright TGFs (i.e. de-  
 217 tectable from space, therefore with more than  $10^{16}$  photons at source) but that shows  
 218 a partially developed RREA spectrum. This is because, for these models, typically  $10^{12}$   
 219 (or more) energetic electrons are initially provided by the cold runaway mechanism. Leader  
 220 models with potential drops as low as  $\approx 160$  MV could potentially produce bright TGFs  
 221 (see Celestin et al. (2015), table 1). By "potential drop", it is meant the potential dif-  
 222 ference between the tip of the lightning leader and the ambient potential.

223 Equation 1 can fit a fully-developed RREA (using  $\epsilon \geq 5$  MeV,  $E_m = 40$  MeV),  
 224 as well as partially developed RREA energy spectra resulting from leader models. The  
 225 leader 300 MV model from Celestin et al. (2015) (figure 3) can be fit by equation 1 with  
 226  $\epsilon = 4.7$  MeV and  $E_m = 30$  MeV as it is close to a fully-developed RREA spectrum.  
 227 The 160 MV leader model can be fit by equation 1 using  $\epsilon = 4.3$  MeV and  $E_m = 20$  MeV.  
 228 In the cases of potential drops of 160 and 300 MV, the initial electron's positions are set  
 229 at 2 meter and 3.5 meter from the leader tip, respectively, because of the shielding of the  
 230 electric field (Skeltved et al., 2017). The corresponding effective electric potential drops  
 231 (i.e. that the energetic electrons can use) are respectively 28 MV, and 53 MV (Celestin  
 232 et al., 2015).

233 In addition to the 160 and 300 MV leader spectra, we chose to test spectra with  
 234  $\epsilon$  equal to 6.5 MeV, 7.3 MeV, 8 MeV and 10 MeV (all using  $E_m = 40$  MeV). The first  
 235 two values correspond to values used in the literature (Dwyer et al., 2012; Bowers et al.,  
 236 2017; Sarria et al., 2018; Xu et al., 2019). After looking at the preliminary results us-  
 237 ing these two values, we decided to add  $\epsilon = 8$  MeV and  $\epsilon = 10$  MeV. These last two

238 values were primarily added on an ad hoc basis, but a physical justification is that, in  
239 theory, non-uniform electric fields in leader models can also produce TGF spectra harder  
240 than typical fully-developed RREA if non-uniform electric fields are involved (Celestin  
241 et al., 2012). We decided not to go above  $\epsilon = 10$  MeV and  $E_m = 40$  MeV, since such  
242 high energies are irrelevant for TGFs.

243 To generate a simulated ASIM spectrum, we proceeded to forward modeling of the  
244 recorded spectrum, using a two stage simulation. In the first stage, a TGF is started at  
245 12 km altitude, assuming one of the initial energy spectra models, and is propagated to  
246 the ISS altitude using the Geant4-based Monte-Carlo model presented in Sarria et al.  
247 (2019) and publicly available (see acknowledgments). Energy, 3D-momentum, and times  
248 of electrons/positrons reaching the ISS within a radius of 80 km (at ISS altitude) are saved.  
249 At the end of this stage, at least 1 million particle records are required for each tested  
250 source TGF spectrum model.

251 In the second stage, the recorded electrons/positrons are used as input of the ASIM  
252 mass model to simulate the response of the instrument. It includes a local geomagnetic  
253 field, and a rotation of frame of reference (Earth to ISS) is applied. The used mass model  
254 includes the ASIM detectors (MXGS, MMIA), the instrument platform, as well as non-  
255 negligible surrounding elements (e.g. the Columbus module). The energy deposition on  
256 the detectors can be direct, i.e. electrons/positrons hitting directly a CZT or BGO crys-  
257 tal, or indirect. In the indirect case, electrons/positrons emit bremsstrahlung photons  
258 by interaction with the surrounding material that hit at least one crystal. Photons can  
259 also come from annihilating positrons, with specific energy of 511 keV. For HED, because  
260 of the shielding, about 98 % of the energy deposition is due to indirect hits into the BGO  
261 crystals. For LED, direct hits are more important: about 72 % of the energy deposition.  
262 This explains why the effective area of LED is larger than HED when considering inci-  
263 dent electrons/positrons. The effective area is calculated as the geometrical area ( $\approx 900$   
264  $\text{cm}^2$  for HED and  $\approx 1024 \text{ cm}^2$  for LED) multiplied by the probability of an incident TEB  
265 electron to deposit more than 300 keV into at least one BGO crystal (for HED), or more  
266 than 50 keV into at least one CZT pixel (for LED).

267 At the end of the second stage, a simulation data set in the form of a list of detected  
268 time and energy counts is generated. To be able to completely neglect the simulation noise,  
269 it is required to have at least 1,000,000 counts on each detector to build each energy spec-

270 trum and calculate the effective areas. The final modeled spectra also include a back-  
 271 ground component build from real background data.

272 A key feature of performing spectral analysis on the TEB, instead of TGF, is that  
 273 the energy spectrum of the constituting electrons and positrons above 100 km altitude  
 274 is only weakly dependent on the following parameters:

- 275 • the radial distance between the TEB center and the ISS. The concept of radial  
 276 is presented more precisely in the supporting information, Figure A.1.
- 277 • the beaming and the tilt angles of the source TGF.
- 278 • the source altitude of the TGF, if set between 10 and 15 km.

279 Actually, we found that the spectrum of the source TGF mostly affects the spec-  
 280 trum of the detected TEB. This permit a substantial simplification of the problem as  
 281 it reduces drastically the number of free parameters to include in the analysis. Since these  
 282 three points are crucial for this analysis, we provide in the supporting information doc-  
 283 ument more detailed arguments and simulation results supporting those three points.  
 284 It includes the results of the procedure described below if applied to source TGF alti-  
 285 tudes of 10 and 15 km, and various opening angle distribution and tilt angles. The ef-  
 286 fect of the source TGF altitude is small and does not affect significantly the results pre-  
 287 sented next (this issue discussed into details in the supporting information, section B).  
 288 In the following, we fix the model to the "consensus" source altitude to 12 km, the an-  
 289 gular distribution to  $\sigma = 20^\circ$ , and the tilt angle to  $0^\circ$ .

290 The simulated spectra are evaluated with respect to the observation, separately for  
 291 the LED (50 to 370 keV) and the HED (0.3 to 40 MeV), and with both detectors together.  
 292 To compare the modeling results to the observation, we use a likelihood analysis, a  $\chi^2$   
 293 analysis (Eadie et al., 1971; Martin, 1971; Lyons, 1986), and the effective LED/HED area  
 294 ratio. Note that these three methods are not independent as they used on the same datasets:  
 295 the list of measured and simulated energy by HED and LED, taken together or separately.

296 For the likelihood analysis, a value of  $-2 \ln(\mathcal{L})$ , the Negative Log-Likelihood, is cal-  
 297 culated. The model with the lowest value of  $-2 \ln(\mathcal{L})$  is considered being the best de-  
 298 scription of the observation. Models are considered to be also possible if their  $-2 \ln(\mathcal{L})$   
 299 values have a difference that is less than a threshold value  $\tau$ . We calculated that  $\tau \approx$   
 300 5 for a confidence level of about 99%, similar to the one used by Mailyan et al. (2016)

301 for Fermi-GBM observations. This value assumes that  $-2\ln(\mathcal{L})$  evolves following approx-  
 302 imately a normal (a.k.a. Gaussian) distribution with respect to the free parameter(s).  
 303 In the following, we present the values  $\Delta_{mle}$ , that are the values of  $-2\ln(\mathcal{L})$  subtracted  
 304 by the value of  $-2\ln(\mathcal{L})$  for the best model. Therefore the best model has  $\Delta_{mle} = 0$   
 305 and compatible models have  $\Delta_{mle} \leq \tau$ . A verification if a given model was found not  
 306 better than another just because of random fluctuations ("by chance") is also performed.

307 For completeness, we also provide a reduced  $\chi^2$  value, noted  $\chi_r^2$ . If  $\chi_r^2$  is below a  
 308 critical value, the model is considered compatible with the measurement, and above the  
 309 model is considered incompatible. The Pearson's  $\chi^2$  method is affected by choice of bin-  
 310 ning (i.e. energy intervals chosen to built the spectra). To mitigate this effect, we chose  
 311 a binning with at least 7 measurement counts on each bin for HED, and at least 10 for  
 312 LED. These two binnings are used to make the spectra presented in Figure 2.b. Given  
 313 the used binning, the critical value  $\chi_{r,c}^2$  is 1.94 (8 degrees of freedom) for LED, 1.75 for  
 314 HED (12 degrees of freedom) and 1.57 for the combination of both (20 degrees of free-  
 315 dom).

316 Compared to the Pearson's  $\chi^2$ , the maximum likelihood analysis presents the ad-  
 317 vantage of not relying on a binning of the measurement data: it keeps all its granularity,  
 318 i.e. no information is lost by binning the measurements. The maximum likelihood anal-  
 319 ysis is better suited than the  $\chi^2$  to estimate which model is the best description of the  
 320 observation (see, for example, Hauschild and Jentschel (2001))

## 321 5 Results and discussion

322 Table 1 summarizes the results of this study. The models are sorted according the  
 323 prevalence of high energies (also called "hardness") or, equivalently, by decreasing LED/HED  
 324 effective area ratio. As indicated in the previous section, three main evaluation criteria  
 325 are presented: the reduced Pearson's  $\chi_r^2$ , the maximum likelihood, and the LED/HED  
 326 effective area ratio.

327 Concerning the LED spectral fits (table 1), all the models give good fits, using the  
 328  $\chi_r^2$  or the Maximum likelihood analysis. We interpret this as the energy range of 50 keV  
 329 to 370 keV being too narrow to discriminate between the models. Concerning the HED  
 330 spectral fits, looking at the  $\chi_r^2$  values, only the 160 MV leader model is found incompat-  
 331 ible. This criterion gives similar conclusions when LED and HED spectra are combined.

332 The maximum likelihood analysis on the HED spectrum indicates that the best model  
 333 is for  $\epsilon = 8$  MeV. The fit for  $\epsilon = 7.3$  MeV is also very close. It indicates that the leader  
 334 300 MV model and harder spectra are also possible explanations. If LED and HED spec-  
 335 tra are combined, the best model is then  $\epsilon = 10$  MeV (but  $\epsilon = 8$  MeV is a very close  
 336 fit here as well), and only models with  $\epsilon = 6.5$  MeV or greater are compatible.

337 Since 307 counts are observed for LED ( $> 50$  keV) and 168 for HED ( $> 300$  keV),  
 338 the observed ratio is 1.83. Considering that the two count numbers individually follow  
 339 a Poisson statistic (but the ratio does not), the uncertainty on the ratio is  $\pm 0.35$  (95%  
 340 interval). It implies that, using this criterion, the two leader-based source TGF spectral  
 341 models (160 MV and 300 MV) are incompatible. The effective area ratio analysis indi-  
 342 cates that the models with  $\epsilon \geq 6.5$  MeV are compatible. In particular we cannot ex-  
 343 clude  $\epsilon = 8$  and  $\epsilon = 10$  MeV. A similar conclusion is obtained with the maximum like-  
 344 lihood analysis (see last paragraph).

345 For this event, TGF spectra harder than previously expected are possible. AGILE  
 346 did report observations of TGF surprisingly hard (up to 100 MeV), but they were later  
 347 found explainable from instrumental effects (Marisaldi et al., 2019). It does not exclude  
 348 that the mechanism presented in (Celestin et al., 2012), used first to explain TGF spec-  
 349 tra up to 100 MeV, could not be responsible for producing TGFs with a bit harder en-  
 350 ergy spectra than fully-developed RREA.

351 The results presented in this article are also only valid for a single event, and it does  
 352 not imply that leader models with potentials of 300 MV or less could explain other TGF  
 353 (and TEB) events. It is also possible that because our method relies on the detection  
 354 of a TEB, we are biased towards a population of strong TGFs, necessitating fully-developed  
 355 RREAs. TGFs that could originate from non-fully-developed RREAs (leader models)  
 356 may never (or very rarely) produce a detectable TEB. This question could be address-  
 357 able in the future, by applying this analysis to more TEB events. We list possibilities  
 358 of new studies in the next section.

359 Finally, table 1 also indicates the positron/electron ratio. The model giving the best  
 360 fit ( $\epsilon = 10$  MeV) gives a ratio of 18.3%, and the range of compatible models give a ra-  
 361 tio ranging from 15.2% to 18.3%. This range is compatible with estimations from the  
 362 Fermi space telescope team (Briggs et al., 2011).

## 6 Conclusions and future work

We reported the observation of a Terrestrial Electron Beam by ASIM on March 24, 2019, originating from the rainbands of the tropical cyclone Johanina. The associated lightning stroke was detected by the GLD360 network (VAISALA) in close temporal association and very close to the ISS's south magnetic field line footpoint. The TEB spectrum was resolved down to 50 keV for the first time, using ASIM's low energy detector. A method to constrain the TGF source energy spectrum based on the TEB detection was presented. It relies on a key reduction of the number of free parameters (altitude, angular distribution, radial distance) possible due to TEB's properties. Comprehensive Monte-Carlo simulations were performed to reproduce the observation, assuming several (energy) spectral shapes of the source TGF. Using three criteria to evaluate the simulation results with respect to the observation (Maximum likelihood, Pearson's  $\chi_r^2$  and LED/HED count ratio), we showed that source TGF with, at least, a fully-developed RREA spectrum  $\propto E^{-1} \exp(-E/\epsilon)$  (with  $\epsilon \geq 6.5$  MeV,  $E_m = 40$  MeV) is compatible with the observation. We could not exclude harder models with  $\epsilon = 8$  MeV ( $E_m = 40$  MeV) and 10 MeV ( $E_m = 40$  MeV), that could potentially be explained by non-equilibrium acceleration of energetic electrons in lightning (Celestin et al., 2012).

In the future, we expect that a larger number of events will be processed using the method presented in this article. For ASIM, it will not be possible before several more years of data gathering, since it currently detects about 4 TEB a year, and not all of them present LED data (only turned ON during the night time of the ISS) or enough counts on LED and HED. In principle, the method presented in this article could also be applied/translated to events from the Fermi GBM TGF/TEB catalog (Roberts et al., 2018), that currently contains about 30 TEB events. Fermi GBM has and high energy (BGO-based) detectors that covers an energy range of  $\approx 150$  keV to  $\approx 30$  MeV. GBM's NaI detectors could also be used in principle (with an energy range of a few keV to 1 MeV) but no TEB spectrum using it was reported yet. Since TEB events present lower fluxes (counts per second) than TGFs (typically 20 times), it makes the spectral analysis much less challenging than for TGF events. Instrumental effects (dead-time, pile-up), affecting TGF analysis, can be mostly (if not totally) ignored for TEB spectral analysis.

Model	Effective area in cm <sup>2</sup>		Effective area ratio	Maximum likelihood analysis result $\Delta_{mle}$			Pearson's $\chi_r^2$			$e^+/e^-$ ratio
	LED	HED		LED	HED	Co.	LED	HED	Co.	
“Leader 160 MV” $\varepsilon = 4.3$ MeV $E_m = 19.2$ MeV	122.0	43.7	2.79	<b>0</b>	19.0	22.5	<b>0.84</b>	1.97	1.66	10.3 %
“Leader 300 MV” $\varepsilon = 4.7$ MeV $E_m = 32$ MeV	141.5	61.0	2.32	<b>0</b>	<b>3.4</b>	7.1	<b>0.88</b>	<b>1.04</b>	<b>1.31</b>	13.3 %
$\varepsilon = 6.5$ MeV $E_m = 40$ MeV	156.0	74.4	<b>2.10</b>	<b>0.2</b>	<b>0.8</b>	<b>3.1</b>	<b>0.89</b>	<b>0.87</b>	<b>1.27</b>	15.2 %
$\varepsilon = 7.3$ MeV $E_m = 40$ MeV	162.2	80.4	<b>2.02</b>	<b>0.3</b>	<b>0.2</b>	<b>1.9</b>	<b>0.88</b>	<b>0.85</b>	<b>1.28</b>	16.1 %
$\varepsilon = 8$ MeV $E_m = 40$ MeV	168.4	85.5	<b>1.97</b>	<b>0.5</b>	<b>0</b>	<b>1.1</b>	<b>0.89</b>	<b>0.84</b>	<b>1.29</b>	16.8 %
$\varepsilon = 10$ MeV $E_m = 40$ MeV	177.8	94.7	<b>1.88</b>	<b>0.5</b>	<b>1.0</b>	<b>0</b>	<b>0.90</b>	<b>0.83</b>	<b>1.30</b>	18.3 %
Compatibility range	<b>n.a.</b>		1.82±0.35	$\leq 5$			$\leq 1.94$	$\leq 1.75$	$\leq 1.57$	<b>n.a.</b>

**Table 1.** Table summarizing the comparison of the tested spectral models with the measurement. Three main criteria are presented: the LED/HED effective area ratio, the maximum likelihood and the Pearson's  $\chi_r^2$ . “Co.” stands for the LED and HED combination. The compatibility range for the different criteria are also indicated. Bold values indicate compatible models for the given criteria (column).

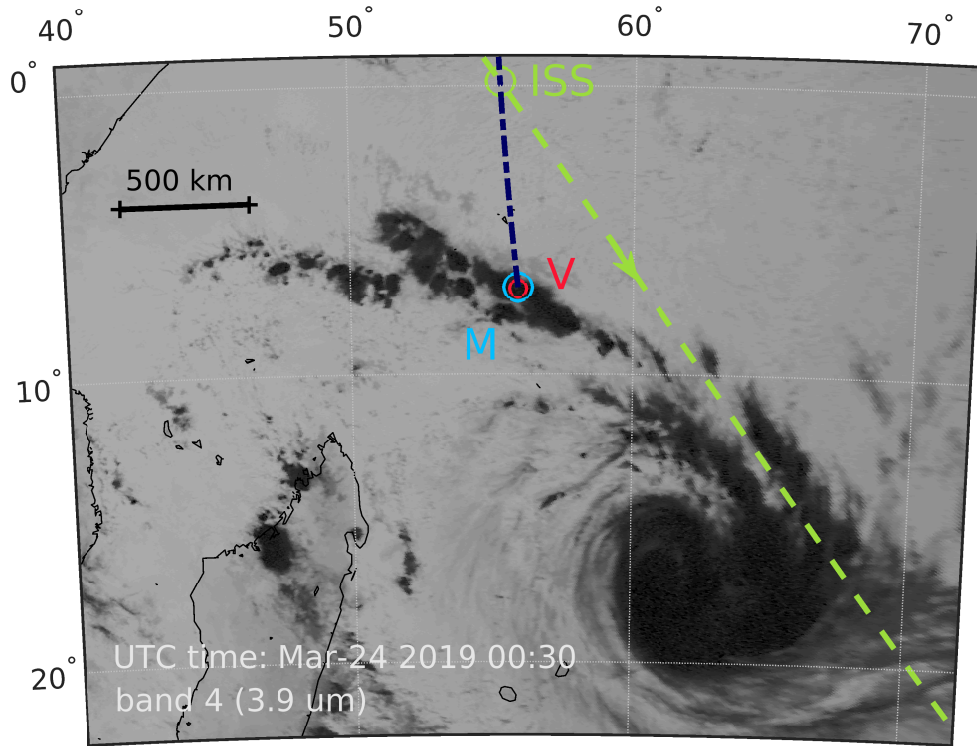


**Figure 1.** Image from geostationary satellite Meteosat-11 around 00:30 UTC, about 1 minute and 53 seconds before the ASIM trigger. The image comes from the optical band 4 ( $3.9 \mu\text{m}$ , 3 km resolution). The tropical cyclone Joaquina can be seen in the south-east part of the picture and extends over a thousand of kilometers. The positions of the International Space Station (ISS), the GLD360 match (V), and the magnetic field line footpoint (M) are indicated. The track of the Earth's magnetic field line (blue dashed line) and of ISS trajectory (green dashed line) are also showed. Point V is very close to M in both location ( $\Delta r = 4.82 \text{ km}$ ) and time ( $\Delta t = 1.44 \text{ ms}$ ), and is located in the north-western rainbands of the cyclone.

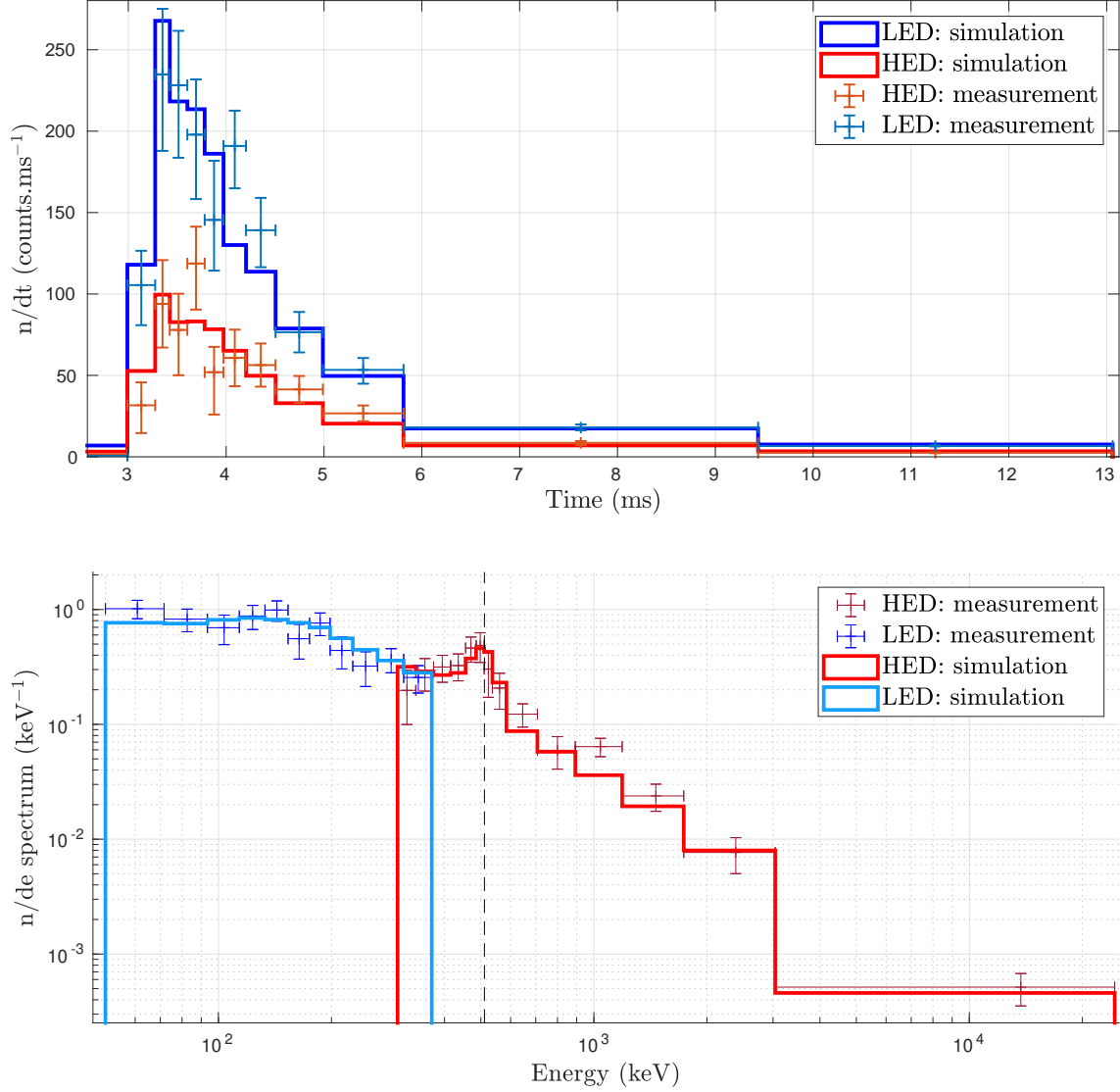


**Figure 2.** ASIM TEB event 190324. **a.** Recorded lightcurve by HED and LED, with  $1\text{-}\sigma$  Poisson error bars. Simulation results from the consensus model are shown and give a good fit to the data ( $\chi_r^2(\text{LED})_t = 1.33$ ,  $\chi_r^2(\text{HED})_t = 1.34$ ). **b.** Recorded energy spectrum by HED and LED, with  $1\text{-}\sigma$  Poisson error bars. Simulation results from the consensus model are shown and give a good fit to the data ( $\chi_r^2(\text{LED})_e = 0.88$ ,  $\chi_r^2(\text{HED})_e = 0.85$ ).

## 393 7 Acknowledgments

394 The data presented in this article is available in the following Zenodo repository:

395 <https://doi.org/10.5281/zenodo.4264459>

396 This work was supported by the European Research Council under the European  
397 Union's Seventh Framework Program (FP7/2007-2013)/ERC grant agreement n. 320839  
398 and the Research Council of Norway under contract 223252/F50 (CoE). ASIM is a mis-  
399 sion of ESA's SciSpace Programme for scientific utilization of the ISS and non-ISS space  
400 exploration platforms and space environment analogues. This study has received fund-  
401 ing from the European Union's Horizon 2020 research and innovation programme un-  
402 der the Marie Skłodowska-Curie grant agreement SAINT 722337. ASIM was funded through  
403 the ESA ELIPS program, through contracts with TERMA and Danish Technical Uni-  
404 versity (DTU) in Denmark, University of Bergen (UB) in Norway and University of Va-  
405 lencia (UV) in Spain. Additional funding was supported by the ESA PRODEX contracts  
406 PEA 4000105639 and 4000111397 to DTU and ESA PRODEX contract 4000102100 and  
407 by Norwegian Research Council to UB. The ASIM Science Data Centre (ASDC) at DTU  
408 is supported by PRODEX contract PEA 4000115884 and by PRODEX contract PEA4000123438  
409 at UB. The ASIM Science Data Centre and data analysis activities at the UV are sup-  
410 ported by the MINECO Research Grants ESP2015- 69909-C5-1-R and ESP2017-86263-  
411 C4-1-R.

412 We thank Vaisala Inc. for access to the GLD360 data. For more information, see  
413 <https://www.GLD360.com/en/products/systems/lightning129detection-networks>.

414 We acknowledge EUMETSAT for making accessible images from the Meteosat-11  
415 geostationary satellite and the MCFETCH service (<https://mcfetch.ssec.wisc.edu/>)  
416 from the Satellite Data Services (SDS) group, at the University of Wisconsin-Madison  
417 Space Science and Engineering Center (SSEC), that is responsible for the access, main-  
418 tenance, and distribution of real-time and archive weather satellite data.

419 The simulations were performed on resources provided by UNINETT Sigma2 - the  
420 National Infrastructure for High Performance Computing and Data Storage in Norway,  
421 under project no. NN9526K.

422 The Geant4-based model for Terrestrial Gamma-ray Flash (TGF) and associated  
423 electrons and positrons propagation in Earth atmosphere and environment (magnetic

424 field) is available in the following GitHub repository: <https://github.com/DavidSarria89/>  
 425 TGF-Propagation-Geant4, or the DOI: <https://doi.org/10.5281/zenodo.2597039>.

## 426 References

- 427 Babich, L. P., Donskoy, E. N., Kutsyk, I. M., & Roussel-Dupré, R. A. (2005). The  
 428 feedback mechanism of runaway air breakdown. *Geophysical Research Letters*,  
 429 *32*(9). doi: 10.1029/2004GL021744
- 430 Bowers, G. S., Smith, D. M., Martinez-McKinney, G. F., Kamogawa, M., Cummer,  
 431 S. A., Dwyer, J. R., . . . Kawasaki, Z. (2017). Gamma Ray Signatures of Neu-  
 432 trons From a Terrestrial Gamma Ray Flash. *Geophysical Research Letters*,  
 433 *44*(19). doi: 10.1002/2017GL075071
- 434 Briggs, M. S., Connaughton, V., Wilson-Hodge, C., Preece, R. D., Fishman, G. J.,  
 435 Kippen, R. M., . . . Smith, D. M. (2011). Electron-positron beams from terres-  
 436 trial lightning observed with Fermi GBM. *Geophysical Research Letters*, *38*,  
 437 L02808. doi: 10.1029/2010GL046259
- 438 Briggs, M. S., Fishman, G. J., Connaughton, V., Bhat, P. N., Paciesas, W. S.,  
 439 Preece, R. D., . . . Chekhtman, A. (2010). First results on terrestrial gamma  
 440 ray flashes from the Fermi Gamma-ray Burst Monitor. *Journal of Geophysical*  
 441 *Research (Space Physics)*, *115*, A07323. doi: 10.1029/2009JA015242
- 442 Celestin, S., & Pasko, V. P. (2011). Energy and fluxes of thermal runaway electrons  
 443 produced by exponential growth of streamers during the stepping of lightning  
 444 leaders and in transient luminous events. *Journal of Geophysical Research*  
 445 *(Space Physics)*, *116*, A03315. doi: 10.1029/2010JA016260
- 446 Celestin, S., Xu, W., & Pasko, V. P. (2012). Terrestrial gamma ray flashes with  
 447 energies up to 100 MeV produced by nonequilibrium acceleration of electrons  
 448 in lightning. *Journal of Geophysical Research (Space Physics)*, *117*(A5). doi:  
 449 10.1029/2012JA017535
- 450 Celestin, S., Xu, W., & Pasko, V. P. (2015). Variability in fluence and spec-  
 451 trum of high-energy photon bursts produced by lightning leaders. *Jour-*  
 452 *nal of Geophysical Research (Space Physics)*, *120*(12), 10,712–10,723. doi:  
 453 10.1002/2015JA021410
- 454 Chanrion, O., Bonaventura, Z., Çinar, D., Bourdon, A., & Neubert, T. (2014). Run-  
 455 away electrons from a ‘beam-bulk’ model of streamer: application to TGFs.

- 456 *Environmental Research Letters*, 9(5), 055003. doi: 10.1088/1748-9326/9/5/  
457 055003
- 458 Chanrion, O., Neubert, T., Lundgaard Rasmussen, I., Stoltze, C., Tcherniak, D.,  
459 Jessen, N. C., . . . Lorenzen, M. (2019). The Modular Multispectral Imaging  
460 Array (MMIA) of the ASIM Payload on the International Space Station. *βr*,  
461 215, 28. doi: 10.1007/s11214-019-0593-y
- 462 Cohen, M. B., Inan, U. S., Said, R. K., Briggs, M. S., Fishman, G. J., Connaughton,  
463 V., & Cummer, S. A. (2010). A lightning discharge producing a beam of rela-  
464 tivistic electrons into space. *Geophysical Research Letters*, 37(18), L18806. doi:  
465 10.1029/2010GL044481
- 466 Dwyer, J. R. (2008). Source mechanisms of terrestrial gamma-ray flashes. *Jour-  
467 nal of Geophysical Research (Atmospheres)*, 113(D10), D10103. doi: 10.1029/  
468 2007JD009248
- 469 Dwyer, J. R. (2012). The relativistic feedback discharge model of terrestrial gamma  
470 ray flashes. *Journal of Geophysical Research (Space Physics)*, 117(A2),  
471 A02308. doi: 10.1029/2011JA017160
- 472 Dwyer, J. R., Grefenstette, B. W., & Smith, D. M. (2008). High-energy electron  
473 beams launched into space by thunderstorms. *Geophysical Research Letters*,  
474 35, L02815. doi: 10.1029/2007GL032430
- 475 Dwyer, J. R., Rassoul, H. K., Al-Dayeh, M., Caraway, L., Chrest, A., Wright, B., . . .  
476 others (2005). X-ray bursts associated with leader steps in cloud-to-ground  
477 lightning. *Geophysical Research Letters*, 32(1).
- 478 Dwyer, J. R., Rassoul, H. K., Al-Dayeh, M., Caraway, L., Wright, B., Chrest, A., . . .  
479 others (2004). Measurements of X-ray emission from rocket-triggered lightning.  
480 *Geophysical research letters*, 31(5).
- 481 Dwyer, J. R., Schaal, M., Rassoul, H. K., Uman, M. A., Jordan, D. M., & Hill,  
482 D. (2011). High-speed X-ray images of triggered lightning dart leaders.  
483 *Journal of Geophysical Research: Atmospheres*, 116(D15), D20208. doi:  
484 10.1029/2011JD015973
- 485 Dwyer, J. R., Smith, D. M., Cummer, S. A., . . . (2012). High-Energy At-  
486 mospheric Physics: Terrestrial Gamma-Ray Flashes and Related Phenomena.  
487 *Space Science Reviews*, 173(1-4), 133–196. doi: 10.1007/s11214-012-9894-0
- 488 Dwyer, J. R., Uman, M. A., Rassoul, H. K., Al-Dayeh, M., Caraway, L., Jerauld, J.,

- 489 ... Wright, B. (2003). Energetic Radiation Produced During Rocket-Triggered  
490 Lightning. *Science*, *299*, 694–697. doi: 10.1126/science.1078940
- 491 Eadie, W. T., Drijard, D., James, F. E., Roos, M., & Sadoulet, B. (1971). *Statistical*  
492 *methods in experimental physics*. Amsterdam: North-Holland. Retrieved from  
493 <https://cds.cern.ch/record/100342>
- 494 Fishman, G. J., Bhat, P. N., Mallozzi, R., Horack, J. M., Koshut, T., Kouve-  
495 liotou, C., ... Christian, H. J. (1994). Discovery of Intense Gamma-  
496 Ray Flashes of Atmospheric Origin. *Science*, *264*(5163), 1313–1316. doi:  
497 10.1126/science.264.5163.1313
- 498 Gjesteland, T. (2012). *Properties of Terrestrial Gamma ray Flashes. Modelling*  
499 *and Analysis of BATSE and RHESSI data* (PhD Thesis, The University of  
500 Bergen). Retrieved from <http://bora.uib.no/handle/1956/6203>
- 501 Gurevich, A. V. (1961). On the theory of runaway electrons. *Sov. Phys. JETP*,  
502 *12*(5), 904–912.
- 503 Gurevich, A. V., Milikh, G. M., & Roussel-Dupre, R. (1992). Runaway electron  
504 mechanism of air breakdown and preconditioning during a thunderstorm.  
505 *Physics Letters A*, *165*(5-6), 463–468.
- 506 Hauschild, T., & Jentschel, M. (2001). Comparison of maximum likelihood estima-  
507 tion and chi-square statistics applied to counting experiments. *Nuclear Instru-*  
508 *ments and Methods in Physics Research Section A: Accelerators, Spectrome-*  
509 *ters, Detectors and Associated Equipment*, *457*(1), 384 – 401. Retrieved from  
510 <http://www.sciencedirect.com/science/article/pii/S0168900200007567>  
511 doi: 10.1016/S0168-9002(00)00756-7
- 512 Kohn, C., & Ebert, U. (2015). Calculation of beams of positrons, neutrons, and pro-  
513 tons associated with terrestrial gamma ray flashes. *Journal of Geophysical Re-*  
514 *search:Atmospheres*, *120*(4), 1620–1635. doi: 10.1002/2014JD022229
- 515 Lindanger, A., Marisaldi, M., Maiorana, C., Sarria, D., Albrechtsen, K., Østgaard,  
516 N., ... Verrecchia, F. (2020). The 3rd AGILE Terrestrial Gamma Ray Flash  
517 Catalog. Part I: Association to Lightning Sferics. *Journal of Geophysical*  
518 *Research:Atmospheres*, *125*(11), e2019JD031985. doi: 10.1029/2019JD031985
- 519 Lyons, L. (1986). *STATISTICS FOR NUCLEAR AND PARTICLE PHYSICISTS*.
- 520 Mailyan, B. G., Briggs, M. S., Cramer, E. S., Fitzpatrick, G., Roberts, O. J., Stan-  
521 bro, M., ... Dwyer, J. R. (2016). The spectroscopy of individual terrestrial

- 522 gamma-ray flashes: Constraining the source properties. *Journal of Geophysical*  
 523 *Research (Space Physics)*, 121(A10), 11. doi: 10.1002/2016JA022702
- 524 Mailyan, B. G., Xu, W., Celestin, S., Briggs, M. S., Dwyer, J. R., Cramer, E. S.,  
 525 ... Stanbro, M. (2019). Analysis of Individual Terrestrial Gamma-Ray  
 526 Flashes With Lightning Leader Models and Fermi Gamma-Ray Burst Mon-  
 527 itor Data. *Journal of Geophysical Research (Space Physics)*, 124(8), 7170–  
 528 7183. Retrieved from [https://agupubs.onlinelibrary.wiley.com/doi/abs/](https://agupubs.onlinelibrary.wiley.com/doi/abs/10.1029/2019JA026912)  
 529 [10.1029/2019JA026912](https://agupubs.onlinelibrary.wiley.com/doi/abs/10.1029/2019JA026912) doi: 10.1029/2019JA026912
- 530 Marisaldi, M., Fuschino, F., Tavani, M., Dietrich, S., Price, C., Galli, M., ... Vercel-  
 531 lone, S. (2014). Properties of terrestrial gamma ray flashes detected by AGILE  
 532 MCAL below 30 MeV. *Journal of Geophysical Research (Space Physics)*, 119,  
 533 1337–1355. doi: 10.1002/2013JA019301
- 534 Marisaldi, M., Galli, M., Labanti, C., Østgaard, N., Sarria, D., Cummer, S. A., ...  
 535 Verrecchia, F. (2019). On the High-Energy Spectral Component and Fine  
 536 Time Structure of Terrestrial Gamma Ray Flashes. *Journal of Geophysi-  
 537 cal Research: Atmospheres*, 124(14), 7484–7497. Retrieved 2021-01-22, from  
 538 <https://onlinelibrary.wiley.com/doi/abs/10.1029/2019JD030554> doi:  
 539 [10.1029/2019JD030554](https://onlinelibrary.wiley.com/doi/abs/10.1029/2019JD030554)
- 540 Martin, B. R. (1971). *Statistics for physicists [by] B. R. Martin*. Academic Press  
 541 London, New York.
- 542 Moss, G. D., Pasko, V. P., Liu, N., & Veronis, G. (2006). Monte Carlo model for  
 543 analysis of thermal runaway electrons in streamer tips in transient luminous  
 544 events and streamer zones of lightning leaders. *Journal of Geophysical Re-  
 545 search (Space Physics)*, 111, 2307. doi: 10.1029/2005JA011350
- 546 Neubert, T., Østgaard, N., Reglero, V., Blanc, E., Chanrion, O., Oxborrow, C. A.,  
 547 ... Bhandari, D. D. V. (2019). The ASIM Mission on the International  
 548 Space Station. *Space Science Reviews*, 215(2), 26. Retrieved 2021-01-  
 549 22, from <http://link.springer.com/10.1007/s11214-019-0592-z> doi:  
 550 [10.1007/s11214-019-0592-z](http://link.springer.com/10.1007/s11214-019-0592-z)
- 551 Neubert, T., Østgaard, N., Reglero, V., Chanrion, O., Heumesser, M., Dimitriadou,  
 552 K., ... Eyles, C. J. (2019). A terrestrial gamma-ray flash and ionospheric  
 553 ultraviolet emissions powered by lightning. *Science*, eaax3872. Retrieved  
 554 2021-01-20, from <https://www.sciencemag.org/lookup/doi/10.1126/>

- 555 science.aax3872 doi: 10.1126/science.aax3872
- 556 Østgaard, N., Balling, J. E., Bjørnsen, T., Brauer, P., Budtz-Jørgensen, C., Bujwan,  
557 W., ... Yang, S. (2019). The Modular X- and Gamma-Ray Sensor (MXGS) of  
558 the ASIM Payload on the International Space Station. *Space Science Reviews*,  
559 *215*, 23. doi: 10.1007/s11214-018-0573-7
- 560 Østgaard, N., Neubert, T., Reglero, V., Ullaland, K., Yang, S., Genov, G., ... Al-  
561 nussirat, S. (2019). First 10 Months of TGF Observations by ASIM. *Journal*  
562 *of Geophysical Research:Atmospheres*, *124*(24), 14024–14036. Retrieved 2021-  
563 01-20, from <https://onlinelibrary.wiley.com/doi/10.1029/2019JD031214>  
564 doi: 10.1029/2019JD031214
- 565 Roberts, O. J., Fitzpatrick, G., Stanbro, M., McBreen, S., Briggs, M. S., Holworth,  
566 R. H., ... Mailyan, B. G. (2018). The First Fermi-GBM Terrestrial Gamma  
567 Ray Flash Catalog. *Journal of Geophysical Research (Space Physics)*, *123*,  
568 4381–4401. doi: 10.1029/2017JA024837
- 569 Rudlosky, S. D., Peterson, M. J., & Kahn, D. T. (2017). GLD360 Performance Rel-  
570 ative to TRMM LIS. *Journal of Atmospheric and Oceanic Technology*, *34*(6),  
571 1307 – 1322. doi: 10.1175/JTECH-D-16-0243.1
- 572 Sarria, D., Blelly, P.-L., & Forme, F. (2015). MC-PEPTITA: A Monte Carlo  
573 model for Photon, Electron and Positron Tracking In Terrestrial Atmo-  
574 sphere—Application for a terrestrial gamma ray flash. *Journal of Geophys-*  
575 *ical Research (Space Physics)*, *120*(5), 3970–3986. Retrieved from [https://](https://agupubs.onlinelibrary.wiley.com/doi/abs/10.1002/2014JA020695)  
576 [agupubs.onlinelibrary.wiley.com/doi/abs/10.1002/2014JA020695](https://agupubs.onlinelibrary.wiley.com/doi/abs/10.1002/2014JA020695) doi:  
577 10.1002/2014JA020695
- 578 Sarria, D., Kochkin, P. O., Østgaard, N., Lehtinen, N. G., Mezentsev, A., Marisaldi,  
579 M., ... Eyles, C. (2019). The First Terrestrial Electron Beam Observed by  
580 the Atmosphere-Space Interactions Monitor. *Journal of Geophysical Research*  
581 *(Space Physics)*, *124*(12), 10,497–10,511. doi: 10.1029/2019JA027071
- 582 Sarria, D., Rutjes, C., Diniz, G., Luque, A., Ihaddadene, K. M. A., Dwyer, J. R.,  
583 ... Ebert, U. (2018). Evaluation of Monte Carlo tools for high-energy atmo-  
584 spheric physics II: relativistic runaway electron avalanches. *Geoscientific Model*  
585 *Development*, *11*, 4515–4535. doi: 10.5194/gmd-11-4515-2018
- 586 Skeltved, A. B., Østgaard, N., Carlson, B. E., Gjesteland, T., & Celestin, S. (2014).  
587 Modeling the relativistic runaway electron avalanche and the feedback mech-

- 588 anism with GEANT4. *Journal of Geophysical Research (Space Physics)*, *119*,  
 589 9174–9191. doi: 10.1002/2014JA020504
- 590 Skeltved, A. B., Østgaard, N., Mezentsev, A., Lehtinen, N. G., & Carlson, B. E.  
 591 (2017). Constraints to do realistic modeling of the electric field ahead of  
 592 the tip of a lightning leader. *Journal of Geophysical Research: Atmospheres*,  
 593 *122*(15), 8120–8134. Retrieved from [https://agupubs.onlinelibrary.wiley](https://agupubs.onlinelibrary.wiley.com/doi/abs/10.1002/2016JD026206)  
 594 [.com/doi/abs/10.1002/2016JD026206](https://agupubs.onlinelibrary.wiley.com/doi/abs/10.1002/2016JD026206) doi: 10.1002/2016JD026206
- 595 Smith, D. M., Grefenstette, B. W., Splitt, M., Lazarus, S. M., Rassoul, H. K., Cole-  
 596 man, L. M., ... Takahashi, Y. (2006). The Anomalous Terrestrial Gamma-ray  
 597 Flash of 17 January 2004. *AGU Fall Meeting Abstracts*, AE31A–1040.
- 598 Smith, D. M., Lopez, L. I., Lin, R. P., & Barrington-Leigh, C. P. (2005). Terrestrial  
 599 Gamma-Ray Flashes Observed up to 20 MeV. *Science*, *307*, 1085–1088. doi:  
 600 10.1126/science.1107466
- 601 Stanbro, M., Briggs, M. S., Roberts, O. J., Cramer, E., Dwyer, J. R., Holzworth, R.,  
 602 ... Xiong, S. L. (2019). A Fermi Gamma-Ray Burst Monitor Event Observed  
 603 as a Terrestrial Gamma-Ray Flash and Terrestrial Electron Beam. *Journal*  
 604 *of Geophysical Research (Space Physics)*, *124*(12), 10580–10591. Retrieved  
 605 from [https://agupubs.onlinelibrary.wiley.com/doi/abs/10.1029/](https://agupubs.onlinelibrary.wiley.com/doi/abs/10.1029/2019JA026749)  
 606 [2019JA026749](https://agupubs.onlinelibrary.wiley.com/doi/abs/10.1029/2019JA026749) doi: 10.1029/2019JA026749
- 607 Ursi, A., Guidorzi, C., Marisaldi, M., Sarria, D., & Frontera, F. (2017). Terrestrial  
 608 gamma-ray flashes in the BeppoSAX data archive. *Journal of Atmospheric and*  
 609 *Solar-Terrestrial Physics*, *156*, 50–56. doi: 10.1016/j.jastp.2017.02.014
- 610 Wilson, C. T. R. (1924). The electric field of a thundercloud and some of its effects.  
 611 *Proceedings of the Physical Society of London*, *37*, 32D–37D.
- 612 Xu, W., Celestin, S., Pasko, V. P., & Marshall, R. A. (2019). Compton Scattering  
 613 Effects on the Spectral and Temporal Properties of Terrestrial Gamma-Ray  
 614 Flashes. *Journal of Geophysical Research (Space Physics)*, *124*(8), 7220–7230.  
 615 Retrieved from [https://agupubs.onlinelibrary.wiley.com/doi/abs/](https://agupubs.onlinelibrary.wiley.com/doi/abs/10.1029/2019JA026941)  
 616 [10.1029/2019JA026941](https://agupubs.onlinelibrary.wiley.com/doi/abs/10.1029/2019JA026941) doi: 10.1029/2019JA026941